PHIPS-HALO: The airborne Particle Habit Imaging and Polar Scattering probe. Part I: Design and Operation

Ahmed Abdelmonem[1], Emma Järvinen[1], Denis Duft[1], Edwin Hirst[2], Steffen Vogt[1], Thomas Leisner[1], and Martin Schnaiter[1]

[1]Institute for Meteorology and Climate Research, Karlsruhe Institute of Technology, Karlsruhe, Germany

[2]Centre for Atmospheric and Instrumentation Research, University of Hertfordshire, Hatfield, AL10 9AB, UK

Correspondence to: A. Abdelmonem (ahmed.abdelmonem@kit.edu), M. Schnaiter (martin.schnaiter@kit.edu)

Abstract. The number and shape of ice crystals present in mixed phase and ice clouds influence the radiation properties, precipitation occurrence and lifetime of these clouds. Since clouds play ~~the~~a major role in the climate system, ~~by~~ influencing the energy budget by scattering sunlight and absorbing heat radiation from the earth, it is necessary to investigate the optical and microphysical properties of cloud particles particularly in-situ. The relationship between the microphysics and the single scattering properties of cloud particles is usually obtained by modeling the optical scattering properties from in-situ measurements of ice crystal size distributions. The measured size distribution and the assumed particle shape might be erroneous in case of non-spherical ice particles. There is a demand to obtain both information correspondently and simultaneously for individual cloud particles in their natural environment. For evaluating the average scattering phase function as a function of ice particle habit and crystal complexity in-situ measurements are required. To this end we have developed a novel airborne optical sensor (PHIPS-HALO) to measure simultaneously the optical properties and the corresponding microphysical parameters of individual cloud particles. PHIPS-HALO has been tested in the AIDA cloud simulation chamber and deployed in mountain stations as well as research aircraft~~s~~ (HALO and Polar 6). It is a successive version of the laboratory prototype instrument PHIPS-AIDA. In this paper we present the detailed design of PHIPS-HALO including the detection mechanism, optical design, mechanical construction, and aerodynamic characterization.

1. Introduction

Better understanding of the radiative impact of different clouds requires knowledge of the link between the cloud microphysics and the single scattering properties of the cloud particles which are used in radiative transfer models. The existing single scattering models like Mie theory usually use the in situ measurements of the ice crystal size distributions as input for optical scattering calculations. Such calculations assume spherical particles to calculate the size distribution from scattering measurements and vice versa. In the past sophisticated optical methods for the computation of the single scattering properties have been developed and applied to non-axisymmetric and irregularly shaped ice particles. These include exact/near exact like T-matrix methods (e.g. (Havemann and Baran, 2001), the Finite Difference Time Domain Method (FDTD) (Yang and Liou, 1999), Discrete Dipole Approximation DDA (Draine and Flatau, 1994;Yurkin and Hoekstra, 2007), or methods based on the geometric optics approximation (Macke et al., 1996), Improved Geometric Optics (IGO) (Bi et al., 2011;Liu et al., 2013;Yang and Liou, 1996), RTDF (Hesse et al., 2009). Despite all these efforts discrepancies remain between cloud radiative properties measured by spaceborne and ground based remote sensing and those driven from in-situ measured microphysical properties (Baum et al., 2010).

A number of airborne in situ instruments were developed to measure particle number concentrations as a function of size evaluated by light scattering. The amount of scattered light is proportional to the particle size and can be modelled provided the knowledge of the shape and refractive index of the particles. A recent overview of different airborne instruments is provided by . The Passive Cavity Aerosol Spectrometer Probe (PCASP) measures side scattered light (~30° to 120°) and covers particle size range from 0.12 to 10μm (Strapp et al., 1992). The Ultrahigh Sensitivity Aerosol Spectrometer (UHSAS) measures also side scattered light but covers size range from 0.06 to 1.0 μm. The Forward Scattering Spectrometer Probes (FSSP) Model 300 measures forward scattered light (from 4° to 12°) and covers size range from 0.3 to 20μm (Baumgardner et al., 1992). PCASP and UHSAS require a deceleration of the particle flow to be able to measure. These instruments measure the intensity of light scattered from individual particles that pass through a focused laser beam. The particle shape is not detected in these measurements. Interpretations of microphysical parameters of cloud particles are usually based on assumptions on the particle shape. Shcherbakov et al. assumed crystals to be hexagonal columns/plates in their modelling approach to retrieve ice particle parameters (Shcherbakov, 2013;Shcherbakov et al., 2006a;Shcherbakov et al., 2006b). The airborne Polar Nephelometer (PN) (Crépel et al., 1997;Gayet et al., 1997) measures the scattering function of the ice particles and was used in conjunction with results from the Cloud Particle Imager (CPI) probe (Lawson et al., 2001) to investigate the impact of the ice crystal habits on the radiative properties of cirrus clouds. This could be done only in a statistical approach with assumptions made on the particle shape within an ensemble of randomly oriented particles.

The PN measures the optical and microphysical parameters of cloud particles in the size range from a few to about 500 μm. The probe measures the scattering phase function of an ensemble of cloud particles intersecting a collimated laser beam near the focal point of a paraboloidal mirror. The light scattered from polar angles from 3.49° to 169° is reflected onto a circular array of 33 photodiodes. The Acquisition rate is selective between 10Hz and 5 kHz. The PN was operated in parallel to the PHIPS-HALO during AIDA cirrus cloud simulation experiments (Schnaiter et al., 2016). The comparison of measurements revealed a reasonable agreement of the two instruments in ice clouds. On the other hand, the CPI records high-definition 2D digital images of cloud particles in the size range from 10μm to 2mm and measures particle size, shape, concentration and individual size distributions for water droplets and ice particles. It has a resolution of 2.3μm and a maximum frame rate of

40 Hz. PHIPS-HALO is a hybrid of those two instruments (PN and CPI) and superiors them by its ability to combine and correlate the optical and microphysical measurements of individual cloud particles. However, the sample statistics of PHIPS-HALO imaging system is limited, particularly for high speed aircraft sampling, due to the very slow sampling rate.

5 (Jourdan et al., 2010) used a principle component analysis (PCA) of the scattering phase function measured by the PN together with particle habits revealed by CPI to link the microphysical and shape properties of cloud particles to their single scattering properties. This link required a clustering of the collected results according to optical parameters of particles and is only true for particles with sizes larger than 50 μm, as the optical contribution of small particles could not be determined directly in a mixed-phase cloud. Measurements of

10 particle morphology are done by some airborne in situ instruments like the Cloud and Aerosol Spectrometer with Polarization (CASPOL) and the Small Ice Detector (SID). The CASPOL measures light scattered by individual aerosol and cloud particles, of sizes from 0.6 μm to 50 μm, in the forward (4° to 12°) and backward (168° to 176°) directions, with an additional polarized detector in the backward direction (Glen and Brooks, 2013;Glen and Brooks, 2014). The particle size is determined by the ~~side~~near forward scattering using Mie theory, and the

15 ~~roughness (or~~ asphericity~~)~~ is determined by the comparison of the signals from two back detectors measuring total and cross-polarized intensities~~at two different angles~~. SID3 measures the spatial light scattering pattern of individual aerosol and cloud particles in forward direction (6° to 25°) for particle sizes range from ~ 1 to 22μm (Kaye et al., 2008;Vochezer et al., 2016). The 2D pattern textures reveal information about the particle roughness as could be shown for laboratory generated ice clouds and mid-latitude mixed-phase and cirrus clouds

20 (Ulanowski et al., 2014;Schnaiter et al., 2016).

Different optical array probes like the Two-Dimensional Cloud (2D-C) probe, the Two-Dimensional Stereo (2D-S) probe and the Cloud Imaging Probe (CIP) have been used to measure the size, shape, and concentration of cloud particles. The 2D-C and CIP record the two-dimensional shadow of the hydrometeor as it passes through a collimated laser beam (Baumgardner et al., 2001;Knollenberg, 1970). The image of the shadow is focused onto a

25 plane containing a linear photodiode array, and the status of the elements of that array is recorded at a rate that permits reconstruction of the image. Compared to 2D-C and CIP, 2D-S uses two orthogonal laser beams crossed in the middle of the sample volume and produces two shadowgraphs on two high-speed linear arrays. The overlap region is defined by the two laser beams to improve the sample volume boundaries and sizing of small particles (smaller than 100μm). The stereo views improve the determination of three-dimensional properties of

30 some particles (Lawson et al., 2006). These optical array probes require the aircraft speed as an input to evaluate the real particle dimensions and to reconstruct a relevant 2D image. Holographic imaging is used in the Holographic Detector for Clouds (HOLODEC) to obtain the size, 2D shadow image and 3D position of every cloud particle coincident in its, particle-size independent, sample volume via digital in-line holography (Fugal et al., 2004).

35

A direct link between the particle habit and the corresponding microphysical parameters is still lacking, at least for complex shapes. Therefore, and for accurate correlation, the microphysical and optical properties of ice crystals have to be measured simultaneously by an in situ instrument.

40 PHIPS-HALO is one of the novel instruments that is developed for the German DLR HALO GV-SP aircraft and certified by Gulfstream, USA. The resolution power of both microscope units is about 2μm. The dual imaging

configuration facilitates a 3D morphology impression of the ice crystals. The scattering unit of PHIPS-HALO allows for the measurement of the polar light scattering function of cloud particles with an angular resolution of 1° for forward scattering directions (from 1° to 10°) and 8° for side and backscattering directions (from 18° to

5 170°). The development of the airborne version (PHIPS-HALO) had ~~some~~ a number of challenges, e.g. the ~~from different types. H~~high particle speed, which may reach to 200m/s due to a carrier like the HALO air-craft, required some special considerations for the aerodynamics and detection mechanism. Data acquisition and storage were required to be included within the same compartment.

2. Basic Instrument Concept

PHIPS-HALO is the aircraft version of the laboratory prototype PHIPS-AIDA, which is described in detail~~s~~ by

10 Abdelmonem et al. (2011)~~(Abdelmonem et al., 2011)~~. Both instruments are successive developments of a prototype particle imager (Schön et al., 2011). This prototype particle imager was ~~completed by~~ upgraded with a second identical imaging unit to image the same particle under different viewing angles and by a polar nephelometer for the simultaneous measurement of the single particle angular light scattering function. The basic measurement concept of PHIPS, therefore, is the simultaneous acquisition of stereo images and the angular light

15 scattering function of individual cloud particles. PHIPS-HALO ~~advances~~ improves upon the other aircraft probes mentioned above with its ability, for the first time, to directly measure the link between the microphysical properties of individual particles and their angular light scattering function. This opens new opportunities to develop and validate single particle light scattering models based on in-situ measurements of atmospheric ice particles.
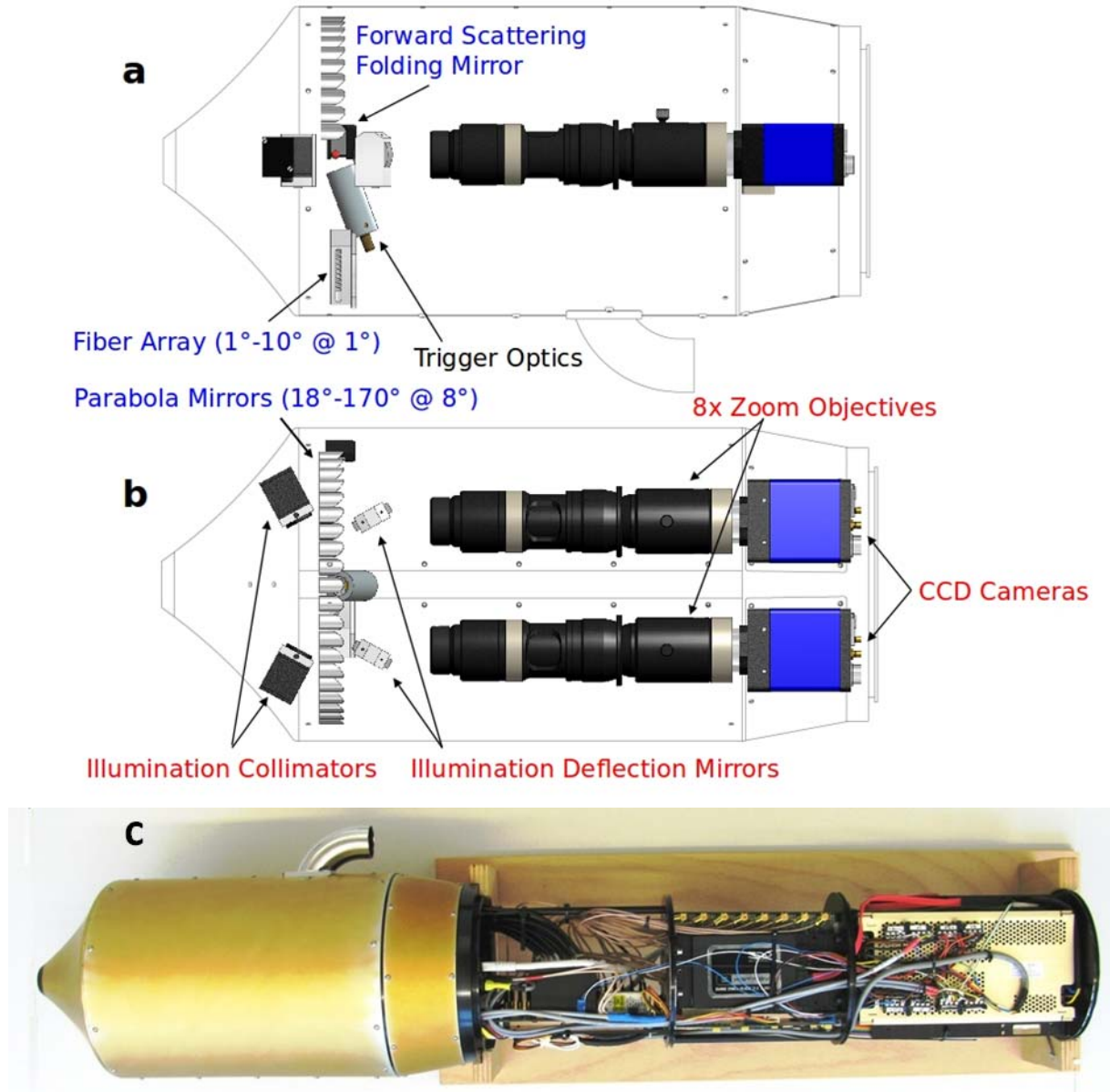
Figure 1: Schematic drawing of the optical detection units used in the PHIPS-HALO probe, (a) side view and (b) top view. The main components of the polar nephelometer and stereo-microscopic imager are labelled in blue and red, respectively. The trigger optics links the two components. (c) A real photo of the probe.

5

The basic idea of the instrument is presented in details in (Abdelmonem et al., 2011) and the basic design of the aircraft version is illustrated in Figure 1. In brief, the optical head of the probe is composed of two combined optical systems. The polar nephelometer part component measures the angular scattered light from individual cloud particles as they intersect a polarized collimated continuous wave laser. Light scattered into the angular

10   range from 1° to 170° with respect to the laser propagation is collected by a specific fiber based optical system (Sect. 3.1.1.), and is measured by a 32 channels Photomultiplier array. One of these channels is used as a trigger input to detect those particles that are in the sensing volume of the instrument. In this way the trigger channel combines the two parts components of the instrument. The second system is a stereo-microscopic imaging system composed of two identical camera-telescope assemblies and a pulsed illumination laser. The two imaging

15   assemblies are separated by an angular distance of 120° to image the same particle from two directions. With

this approach, ~~a~~ three dimensional information of the particle shape and its orientation with respect to the scattering laser can be inferred. The particles are illuminated by the flash laser using a Y-like fiber optic and two optical collimators. Bright field micrographs of the particle are imaged on the CCD of each camera. Both optical systems are controlled by an electronic assembly. This electronic assembly (i) triggers the light scattering measurement and the image acquisition and, (ii), processes the scattering signals. The electronic assembly is described in Sect. 3.2.

The major difference between the aircraft and laboratory versions is the compact, light and streamline design of the aircraft version. In addition, a ~~specifically~~ specially developed compact electronic assembly, by the University of Hertfordshire - UK, is used to control the optical systems of PHIPS-HALO. Other important differences are mentioned below within the context of the discussion.

3. Set-Up

3.1. Optical Head

All structural parts of PHIPS-HALO are made of Aluminum AA6060 or AA7075. The covering parts of the optical head are made of DURAL-sheet metal (AA2024). The optical head has a cylindrical shape with an outer diameter of 203mm and a length of 465mm. The sample flow outlet ~~extents~~extends the head diameter by 51mm. The outlet faces the ground when the instrument is attached to the aircraft. The volume of the optical head is divided by the main optical plate ~~where~~ to which different components are ~~fixed to~~attached. The stereo-microscopic imaging system and the air outlet tube are fixed on one side of the main optical plate while the trigger detector, the scattering laser and the flash laser are fixed on the other side. The front part of the optical head is composed of a ~~specifically~~ specially designed inlet. It has a clear diameter of 30mm at the front most and 32mm at the detection volume side and a length of 98mm. The main task of this inlet is to transfer cloud elements to the sensing area of PHIPS-HALO with a minimum disturbance of their thermodynamic state. All optical components are heated to temperatures above the dew point to avoid water condensation on optics or ice aggregation which may clog the air path.

3.1.1. **PHIPS-HALO** Polar Nephelometer

The polar nephelometer, Figure 1, consists of the front optical ring, back optical ring, 20 off-axis parabolic mirrors (Kaleido Technology, EFL=15, CA=10mm), 20 individual fiber couplers, forward scattering mirror, forward scattering coupler for 10 fibers, 30 PMMA optical fibers of 600μm diameter and 0.39 numerical aperture (not included in drawings for clarity), scattering laser beam steerer, trigger optics, and scattering laser source. The scattering laser is a frequency doubled Nd:YAG laser (CrystaLaser, model CL532-300-L) with a wavelength of 532 nm, an output power of 300mW, a beam waist of 0.36 mm, and a beam divergence of 2mrad and a beam pointing stability of less than 0.02mrad. The emitted radiation is linearly polarized with a polarization direction vertical to the base plate of the laser head. The plane of scattering of the polar nephelometer is perpendicular to the main optical plate and includes the center of scattering of the detection volume which is 20mm above the optical plate and coincides with the central axis of the inlet tube. The scattering plane is a virtual plane lies between the two optical rings at a distance of 10 mm from the back optical ring and includes the scattering center and the off-axis parabolic mirrors. The off-axis parabolic mirrors, which

replace the collimating lenses in the laboratory version, are fixed to the optical ring and have their field of view at the detection volume. The CW green laser beam of the scattering laser source is steered by a beam steerer, fixed between the two rings, to the plane of imaging and travels along the axis of intersection between the plane of imaging and the plane of scattering. The beam passes through the detection volume to the forward mirror and then reflected to a beam dump in the forward scattering coupler which is fixed on the back optical ring. This path defines the 0° of the polar scattering angular distribution. The forward coupler has 10 holes after the beam dump positioned at equidistant angular separations of 1° (i.e. from 1° to 10°) and is placed at a scattering distance of 200mm from the scattering center. The 20 off-axis parabolic mirrors are placed at equidistant angular separations of 8° (from 18° to 170°) and a scattering distance of 83mm. They are fixed to the first ring on a virtual arc of diameter 83mm. The scattered light sampled at the angles between 18° and 170° is reflected and focused by the parabolic mirrors to the fiber couplers. 30 fiber optics are coupled to the forward coupler and the individual fiber couplers and connected to the multi-anode photomultiplier array (MAPMT, Hamamatsu, model H7260) in the electronic part of the probe.
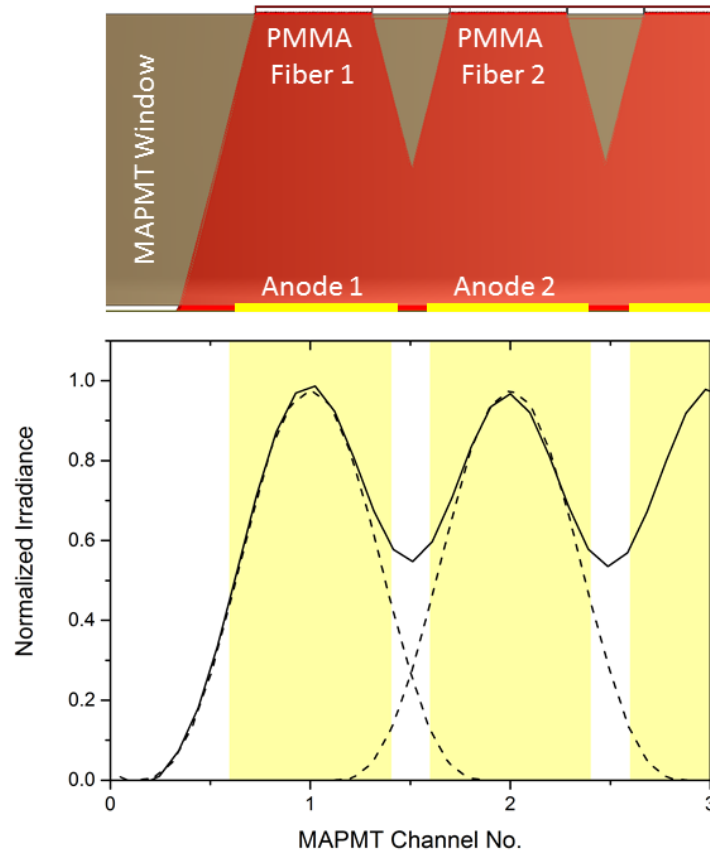

Figure 2: Results of optical modeling calculations for the light coupling between the PMMA fiber system and the multi-anode photomultiplier. A crosstalk of at least 15% can be expected that needs to be taken into account in the analysis of the polar nephelometer measurements.

Optical design calculations were performed to define the specifications of the fiber system that couples the scattered light collected by the polar nephelometer to the MAPMT. These calculations were performed by using the optical engineering software FRED (Photon Engineering, LLC, USA). Based on the results of these calculations, an optimum distance between the fiber end and the off-axis parabolic mirror of 16mm was found

that reduces the focal spot to a reasonably small diameter. Further, the numerical aperture of the off-axis mirrors was specified to be smaller than the numerical aperture of the fibers which is the second requirement for a good coupling. The modeled coupling between the fiber end and the MAPMT is shown in Figure 2. The optical modeling shows that a residual crosstalk between the individual channels of about 2015% can be expected, even though the fibers are placed close the protection borosilicate window of the MAPMT. This crosstalk was verified by successively coupling laser light from an integrating sphere into the individual fibers while the other fibers were blocked. The result of this laboratory characterization of the MAPMT is shown in Figure 3.
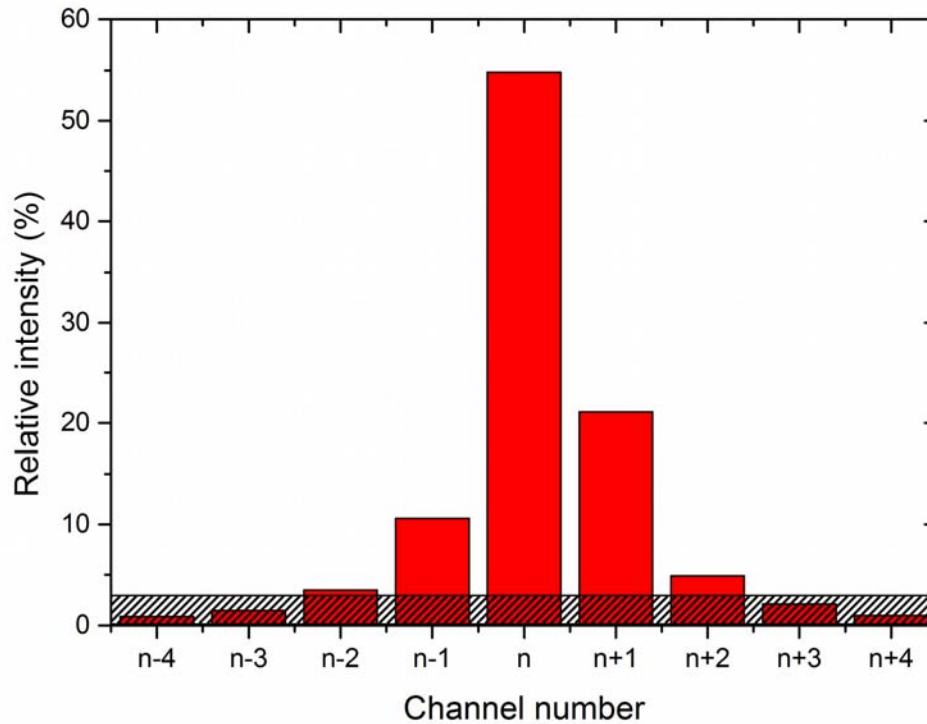

Figure 3 Results of the laboratory characterization of the optical crosstalk within the MAPMT of PHIPS-HALO. The manufacturer given electronic crosstalk between adjacent detectors of 3% is indicated by the shaded area. The deduced optical crosstalk between adjacent detectors is 10% to the left and 20% to the right side indicating a slight misplacement of the fiber coupler with respect to the MAPMT.

To minimize the influence of this crosstalk onto the measurement, (i) the fibers were arranged in a respective order, i.e. the angular arrangement is mapped on the MAPMT, and (ii) channel 106° is placed next to the trigger channel (channel 1 of the MAPMT). The latter point was necessary to avoid the instrument to trigger on particles outside the sensing volume via crosstalk sensitivity. The strong angular variability of the scattering intensity is shown in Sect. 5, where calculated scattering intensity functions are presented.

3.1.2. Stereo-Microscopic Imager

Two camera-telescope assemblies are placed after two reflecting mirrors to image the detected particle at two different viewing angles with respect to the particle path inside the probe, +60° and -60° (in contrast to +30° and

-30° in the laboratory version) from the central axis of the probe). The imaging plane is defined by the scattering centre and the two camera-telescope assemblies and is perpendicular to the scattering plane. Two identical cameras (GE1380, Allied Vision Technologies Inc., Canada) are used with a 2/3 inch 12bit CCD sensor, an image resolution of 1360 x 1024 pixels, a pixel size of 6.45 μm x 6.45 μm, a maximum frame rate of 20Hz, a trigger delay of about 4μs, and a trigger jitter of ±30ns. Microscopic images are ~~generated~~ projected on~~to~~ the CCD sensors by using zoom objectives (Zoom 6000, Navitar Inc., USA) with a variable magnification from 1.4 to 9.0, which corresponds to a field of view range~~s~~ from 6.27 x 4.72 mm to 0.98 x 0.73 mm ~~7.86mm to 1.22mm (diagonal size)~~, respectively. The optical resolution ranges from 7.2um to 2.35um for the low (1.4X) and high (9.0X) magnification, respectively. A typical operating optical resolution is ~5.3μm (at 4X magnification) with a field of view ~ 2.19 x 1.65 mm. The corresponding particle size range is from ~10 μm to 1.5 mm. The imaging system is calibrated with a calibration slide before each campaign and after any change of the telescope magnification~~-~~. The objectives have a nominal working distance of 92mm. The image of a ~~detected~~ cloud particle is casted on the CCD ~~illuminated~~ by freezing the motion of the particle using a ~~an~~ 40 ns incoherent pulsed diode laser (Cavitar, model Cavilux, 690nm, 400W, Class 4) ~~to~~ produc~~e~~ing a bright field microscopic image~~s~~. In contrast to the ultrafast flash lamp used in the prototype version, the incoherent flash laser improves the homogeneity of the image background and the quality of the image due to the high pointing and power stabilities and prevents the chromatic aberrations. The incoherency ~~refrains~~ avoids ~~from~~ the formation of interference patterns at the CCD. A long-pass filter (THORLABS, FEL0600) is used to prevent the scattered light from disturbing the captured images. The incoherent flash laser and its controller are attached to the optical plate at the other side from the camera-objective assemblies. The illumination light is transmitted to the detection volume using a Y-like optical fiber (2mm to 2x1mm diameter) coupled to a 90° telescope which collimates the light and aligns it along the axis between the detection volume and camera telescope. The particle is reproduced as a bright field microscopic image on the CCD of each camera. The two images for the same particle at two different angles give a sense of the 3D morphology in a similar manner to the human stereo vision. The reconstruction of the full 3D shape is possible for regular geometric shapes like rods, columns, plates, etc. (Abdelmonem et al., 2011). Aside from that, the investigated parameters can be compared and/or averaged. For example, the larger (or smaller) value of particle size deduced from the two corresponding particle perspectives of plates, columns or complex irregular particles (e.g. rosettes, stars) can be specifically selected in order to reduce the width in the averaged particle size distribution.

Since PHIPS-HALO is a hybrid of the PN and CPI instruments and combines and correlates the optical and microphysical measurements of individual cloud particles, we show a comparison between the polar nephelometer of PHIPS-HALO and the PN instrument in Table 1 and a comparison between the stereo-microscopic imager of PHIPS-HALO and the CPI probe in Table 2.

Parameter Instrument	PN Instrument	PN of PHIPS-HALO
Detection target	Ensemble of cloud particles (water droplets or ice crystals)	Individual cloud particles (water droplets or ice crystals)
Particle size range	Few to 500 μm	few μm to a few hundred μm
No. Of measuring channels	33	30 + 1 for trigger
Polar angles range and resolution	Range: 3.49° to 169° Resolution: 0.79° (from 3.49 to	Range: 1° to 170° Resolution: 1° (from 1° to 10°) and

	9.02), 1.58° (from 9.02 to 10.6) and 7° (from 15 to 169.5)	8° (from 18° to 170°)
Acquisition rate	10 Hz or 5 kHz.	9 kHz
Signal coupling	One paraboloidal mirror for all channels. 10 fibres to photodiode for the forward direction 23 photodiodes for the side and backward directions	10 direct incidence on fibres for the forward direction and 20 off-axis parabolic mirrors and fibres for the side and backward direction

Table 1: The specifications of the PN component of PHIPS-HALO compared to those of the PN instrument

Parameter　　　　　　Instrument	CPI Probe	Stereo imager of PHIPS-HALO
	2D imaging (one camera)	Stereo imaging (two cameras)
Particle size range	10µm to 2mm	10 µm to 1.5 mm (typical range at 4X magnification) ~3 µm to ~4.7 mm (magnification dependent)
Resolution	2.3 µm	~ 2.35 µm (Max.)
Maximum frame rate	40 Hz	20 Hz
Image casting	25 ns pulsed laser diode	40 ns pulsed incoherent laser diode

Table 2: The specifications of the stereo-imager component of PHIPS-HALO compared to those of the CPI probe

3.2. Electronics and Signal Processing

The electronics of PHIPS-HALO comprises the MAPMT and amplifier board, four analogue signal conditioning and 12bit analogue-to-digital converter boards, and the backplane and control board. Particle data acquisition is controlled by a FPGA controller located on the backplane board, and communication with the host computer is via the USB daughter board mounted on the backplane. The FPGA controls all the functions of the electronics. It sequences the control signals to the peak detectors and analogue-to-digital converters when a particle event is triggered and then stores the returned data in the FIFO. At approximately 0.7s intervals, the FPGA stores a particle data set irrespective of whether it has been triggered or not. This forced triggered data can be used to get a continuous record of the background signals of the polar nephelometer channels. On a real particle event a signal is generated from the control board to trigger the PHIPS-HALO cameras and the illumination laser. The delay between these two triggers is programmable up to 10µs to take into account the camera shutter latency. The triggers are disabled when the camera busy signal is asserted.
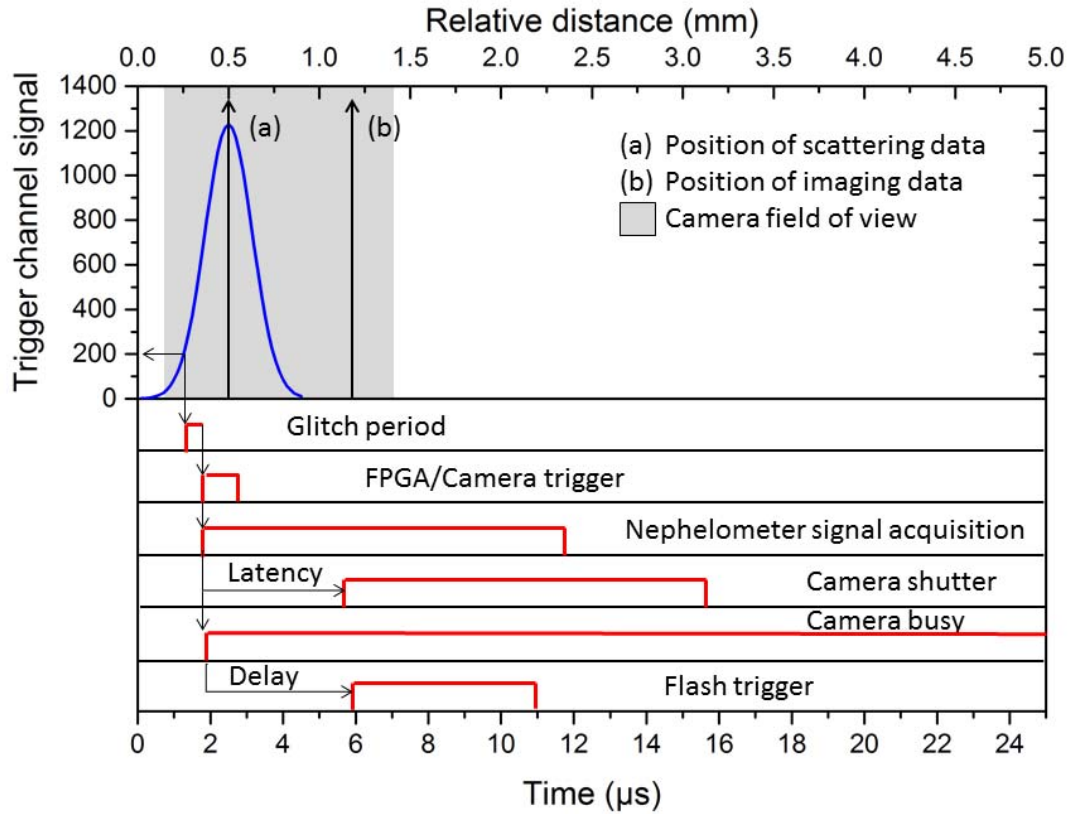
Figure 4: Signal detection and processing scheme for a valid particle event at a typical airspeed of 200m/s and at an assumed trigger threshold of 200. The relative distance along the particle trajectory, i.e. the instrument axis, is given on the upper axis. Note, that due to the camera field of view of 1.27 mm along the instrument axis, the imaging system can be aligned in the laboratory by using test particles with particle speeds of only a few m/s.

Figure 4 shows the schematics of the signal detection and processing sequence for a valid particle event. When a particle passes the field of view of the trigger channel, a light pulse is generated on channel 1 of the MAPMT. The analogue trigger signal (panel a of Figure 4) is routed to a comparator that is used to generate a TTL trigger for initiating the data acquisition sequence controlled by the FPGA. The comparator is checking whether the following conditions are fulfilled by the signal: (i) the signal is above a certain threshold set by the FPGA, and (ii) the signal has stayed above this threshold for a certain time period to be insensitive to glitches. The latter is also set by the FPGA in clock-cycle units of the electronics which is 48MHz, i.e. about 21ns. If both conditions are fulfilled, the FPGA gets a valid particle trigger signal. The FPGA then immediately sends a trigger signal to the cameras to open the shutter. As the cameras have reliable trigger latency times of 3.9μs, a period of at least 4μs is awaited before a second trigger is ~~send~~ sent to the flash laser that illuminates the particle with a pulse of ~~10ns~~40 ns. The delay between the particle event detection by the electronics and the particle imaging results in a relative distance of about 0.7mm between the positions along the particle trajectory where the scattering and imaging data are taken. However, a significant change of the particle orientation with respect to the scattering plane during this delay is unlikely as this would require unrealistically high particle angular rotation speeds of the order of 1 kHz.

11

4. Modeling of the Aerodynamic Properties of the Instrument Head

As mentioned above, the probe is ~~assumed~~ designed to fly with a speed of 200m/sec at an altitude up to 16km and temperatures below -60°C. An aerodynamic study was necessary to estimate the mechanical ~~solidity~~ stability of the probe and to verify the geometry for a turbulence-free detection volume. To this end, CFD simulations were carried out using ANSYS CFX 15.0 to evaluate the temperature, pressure and velocity distributions inside and outside the probe.

To reduce computational effort and improve solution stability the original complete CAD model of the probe has been simplified to include only the crucial geometrical features influencing the flow field. Smaller features as screws and cables as well as objects further away from the open paths are omitted. Additionally mirror symmetry with respect to the y-z-plane was applied. Shear Stress Transport with automatic wall function and high speed compressible wall heat transfer option was used as the turbulence model on a non-buoyant domain using air ideal gas as the fluid. The radial boundary was set as an opening with activated Zero Gradient Turbulence Option. ~~The model was run with an inlet normal velocity of 200m/s with low intensity turbulence at a pressure of 187mbar and air temperature of 227K~~ The model was run with input parameters reflecting the range of operation conditions during typical flights of the HALO and Polar 6 aircrafts. In the following the results of a simulation employing 187mbar ambient pressure and 227K air temperature and 200m/s flight speed are shown. ~~The radial boundary was set as an opening with activated Zero Gradient Turbulence Option.~~

4.1. Flow velocity and Mach Number

As a basic requirement for overall stability of the probe and to minimize structural stress on the probe as well as on its mount and the airplane, supersonic speeds of the flow field around the probe should be avoided. Figure 5 shows the modelled Mach number distribution which is the ratio of relative local air speed to the speed of sound inside and outside the probe at a flight speed of 200 m/sec. The simulation shows that Mach numbers are generally below 0.8 with maximum values as high as 0.9 at the outer edges of the probe. However, the speed of sound (MN=1) is not reached or exceeded.

The static mechanical stress on the probe can be estimated from the pressure data shown in lower panel of Figure 5. Due to the open design the inside of the probe has an overall average pressure elevated by 8 hPa compared to the background pressure. At probe front tip and front edge higher pressure differences of 56 hPa and -79 hPa occur. This is sustainable with the lightweight aluminum-structure of the probe under static conditions.
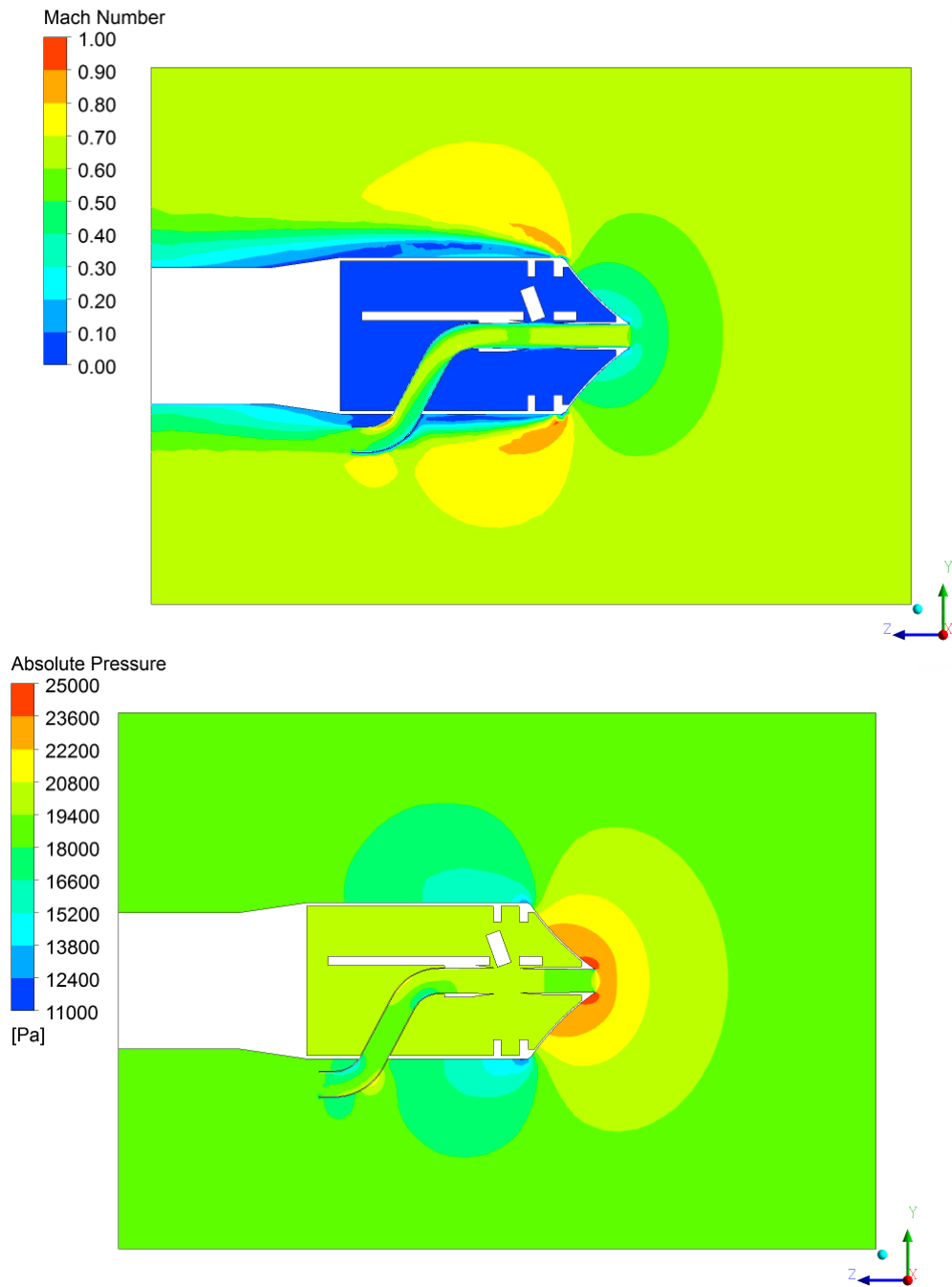
Figure 5: Mach number distribution (upper panel) and pressure distribution (lower panel) of the flow field inside and outside the probe.

5

4.2. Temperature

To make sure that pristine and unaltered particles are measured within the detection volume, the temperature along the particle trajectories is important. The temperature distribution inside and outside the probe is shown in the upper panel of Figure 6. The simulation along the particle trajectory crossing the detection volume in the lower panel shows, that the particles experience a short-term temperature change due to adiabatic heating of the surround air which lasts for about 1ms and gives rise for a period of subsaturation and particle evaporation. Basic diffusion growth theory (e.g. (Pruppacher and Klett, 1997)) can be used to estimate the mass loss for an ice particle during this period of non-equilibrium conditions. For simplicity, the ice particle is assumed to be spherical for this estimation. The calculation shows, that a d=2 µm particle reduces its size by about 5 nm through evaporation corresponding to a mass loss of $\Delta m/m = 0.8\%$, whereas a d=10 µm particle shrinks by less than 1 nm ($\Delta m/m = 0.01\%$). This dependence on particle size originates from the fact, that due to their larger mass and thus increased heat capacity, larger particles do not accommodate quickly enough to the ~~fast~~ rapidly changing temperature of the surrounding air. The lower particle temperature directly results in a lower evaporation rate. In conclusion, very small ice particles of d=2 µm and below will experience a short term evaporation of a few mass percent at maximum. Larger particles will essentially be unaffected by the short term heating. The modelled pressure and temperature increases due to compression at the probe tip are in a very good agreement with the values given in (Weigel et al., 2015) which are based on temperature, pressure, and velocity measurements on the nose boom of the HALO aircraft and the underwing cloud probes.
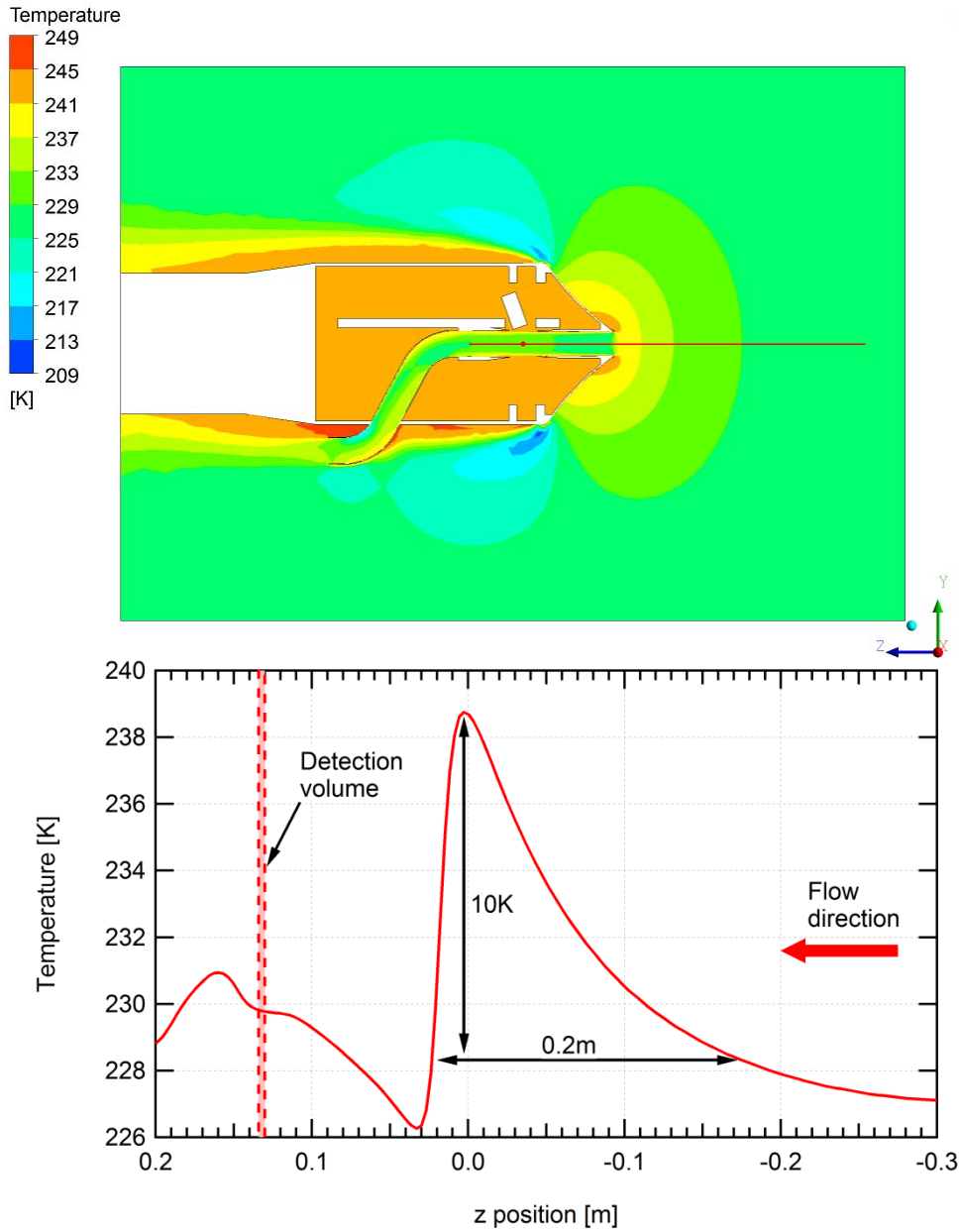
Figure 6: Temperature distribution inside and outside the probe (upper panel) and along the centre line trajectory (lower panel). Incoming particles experience a short-term temperature change of the surrounding air by about 10K within 1 ms at 200 m/s flight speed.

4.3. Turbulence

Another important parameter for the correct operation of the probe is to estimate whether the degree of turbulence ice particles experience on their path ~~from the undisturbed air outside~~ towards the detection volume. The upper panel of Figure 7 shows the distribution of Turbulence Kinetic Energy (TKE) which is the kinetic energy per unit mass associated with eddies in turbulent flow. The square root of the TKE is a measure of typical velocities associated with the turbulent fluctuations. The typical turbulent velocity close to the walls of the air channel is about 10m/s being sufficiently low that potential ice crystals originating from the turbulent region close to the wall do not enter the sample volume and only unperturbed crystals are detected. The TKE along the

15

center line trajectory is shown in the lower panel of Figure 7 reaching a value of about 0.7 m²/s² at the detection volume (red square). This corresponds to typical turbulent velocity of about 0.8 m/s which should be low enough to not destroy primary i.e. not-aggregated cirrus cloud ice crystals. ~~However, larger cloud particles consisting of weakly bound aggregates could potentially disrupt. No conclusions can be drawn from this analysis about ice crystal shattering at the probe inlet tip.~~
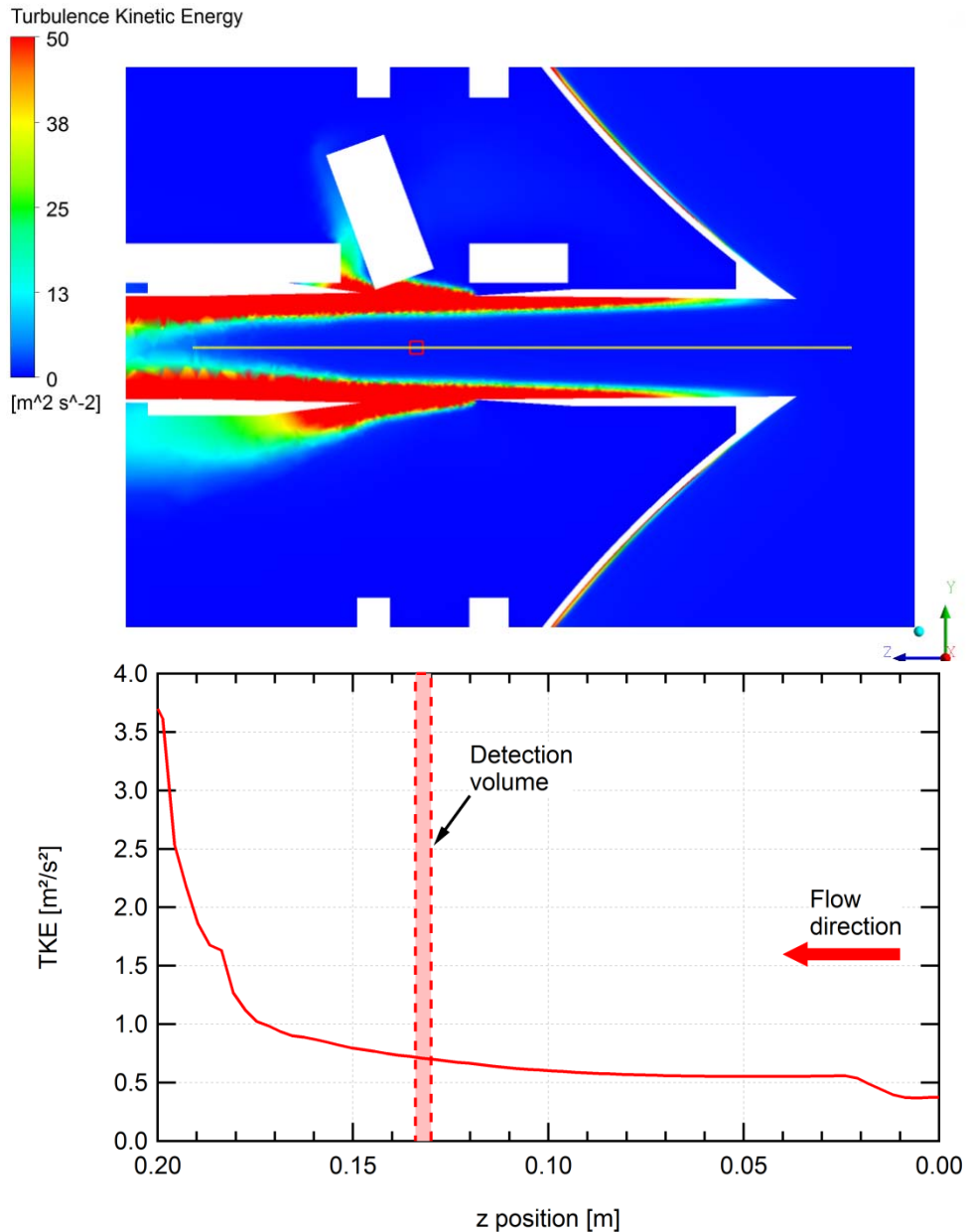

Figure 7: Upper panel: Turbulence Kinetic Energy distribution within the particle flow tube of the probe. The red square marks the detection volume. Lower panel: The TKE along the horizontal centre line trajectory (shown above) is only slightly increased compared to the background value.

To verify that the probe may be operated at a variety of conditions different from the above scenario several simulations have been performed which reflect the typical range of conditions encountered with the HALO and Polar 6 aircraft~~s~~. For the operation of the probe, the most important simulation results are the degree of

turbulence at the detection volume, the temperature change cloud particles experience along the trajectories to the detection volume and the estimated mass loss due to evaporation. The results along with the flight parameters are given in Table 3. The first case corresponds to the simulation shown before. The results confirm the conclusions drawn in the analysis above. Turbulence induced by the flow at the probe inlet walls does not propagate to the detection volume due to the speed of air inflow. The degree of turbulence at the detection volume is thus only slightly elevated to the background value for all conditions. The maximum temperature difference cloud particles experience along their trajectory to the detection volume clearly depends on the speed of the aircraft and is thus highest at the maximum flight speed of ~~250~~240 m/s of the HALO aircraft. Nevertheless, even at high speed the mass loss due to evaporation is below 0.1 % for ice particles with a diameter of 10 μm and above.

Flight type	Flight parameters			Results				
	p [bar]	v [m/s]	T [K]	TKE [m²/s²]	ΔTmax [K]	Δm/m [%] d=2μm	Δm/m [%] d=10μm	Δm/m [%] d=15μm
HALO								
Typical	0.187	200	227	0.7	11.8	0.8	0.01	0.003
Low altitude	0.~~78~~419	~~200~~110	256	~~0.3~~0.2	~~12.4~~3.0	~~2.4~~1.6	~~0.05~~0.04	~~0.001~~0.01
~~Maximum speed~~High altitude	~~0.187~~0.129	~~250~~240	~~227~~221	~~1.5~~1.7	~~20.0~~18.3	~~1.5~~1.0	~~0.02~~0.01	~~0.004~~0.003
Polar 6								
Typical	0.78	75	256	0.06	1.4	0.6	0.02	0.006

Table 3: Simulation results for different model settings corresponding to possible flight conditions. Turbulence kinetic energy at the detection volume (TKE), maximum temperature difference along the center trajectory (ΔTmax), estimated mass loss due to evaporation (Δm/m) for three different cloud ice particle diameters.

Ice particle shattering may significantly affect the measurements of any airborne particle probe. The shattering of cloud particles at the inlet of the probe is not discussed here; however, the nozzle of the instrument is designed with a very sharp edge to minimize the probability of collision with that edge. The advantages of sharp tip and probe-inlet design with respect to minimizing shattering are described in details by (Korolev et al., 2013). Particles hitting the outer part of the tip are forced to follow a trajectory outside the instrument. Shattering out of collisions with the inner walls of the inlet is greatly reduced due to the straight design of the inlet. In addition, the inlet has been designed with ~~an~~a slowly expanding diameter (from 30mm at the front tip to 32mm at the detection volume side) which further reduces the probability of particle shattering.

5

To evaluate the sensitivity of the probe design to non-zero angle of attack (AoA) conditions, a series of simulations has been performed under varying attack angles. It was found that the level of turbulence in the detection volume is not influenced significantly for AoA below 4°. For higher AoA the level of turbulence in the detection volume increases rapidly as the turbulence which originates from the inlet walls reaches to the detection volume. In reality the angle of attack of the HALO aircraft is not constant but depends on air speed and ranges between 1.5° and 6.5° during typical flights covering low and high altitudes. This range of AoA is partially compensated by a pre-tilted probe mount (2.8° nose down) such that the AoA on the probe is in the range of -1.3° to +3.7° which is well within the limits of ±4°. At the most typical air speed of about 200m/s the AoA on the probe is within ±1°. More details on the AoA study are given in the supplementary information.

10

5. Modeling of the Instrument Response and Detection Range for the Scattering Optics

The PHIPS-HALO probe is designed to image water and ice particles in mixed-phase clouds and ice crystals in cirrus clouds, where the diameter of these particles can range from few microns to several hundred microns. Simultaneously, the scattering optics measures the scattering phase functions of the imaged particles. The difficulty in the scattering measurements is that a high dynamic range is needed for the detectors, as the ~~amount of intensity~~ intensity of light reaching them can range several orders of magnitudes depending on the laser power, detector geometry and the particle microphysics.

To determine the sensitivity threshold and the dynamic range of the polar nephelometer ~~part~~ component of the PHIPS-HALO instrument, we modelled the response of the detectors to scattering ~~of~~by spherical particles. The total power that arrives ~~to~~ through the solid angle of a detector from scattering ~~of~~ by a sphere with known refractive index is dependent on the incident laser intensity, on the distance of the detector to the scattering center and on the detector geometry through the following equation

$$P(\theta) = \frac{I_0}{4\pi r R^2} \iint_A \frac{dC_S}{d\Omega}(d,\theta) d\Omega, \qquad (\text{x1})$$

where I_0 is the laser intensity, R the distance from scattering centre to the detector, Ω the solid angle of the detector and $\frac{dC_S}{d\Omega}(d,\theta)$ the differential scattering cross section of a particle with diameter of d. Since the detector areas are spherical for both forward direction fibres and for the parabolic mirrors in the sideward direction, the double integral (x1) can be analytically solved with respect to the azimuthal angle, and the resulting integral depends only on the polar angle as follows

$$P(\theta) = 2I_0 \int_{\theta_0-\alpha}^{\theta_0+\alpha} \frac{dC_S}{d\Omega}(d,\theta) \sin\theta \arctan\sqrt{\tan^2\alpha - \tan^2(\theta-\theta_0)}\, d\theta, \qquad (\text{x2})$$

where α is the half opening angle of the detector (arctan(r/R)). The scattering cross section of the spherical particles can be calculated using ~~the~~ Mie-theory (for this Bohren and Huffman code was used,(Bohren and Huffman, 2007)) and for vertically polarized laser the scattering cross section can be expressed as following

$$\frac{dC_S}{d\Omega}(d,\theta) = \frac{|S_1|^2}{k^2}. \qquad (\text{x3})$$

The theoretical power measured by a detector (nW) was calculated for five droplets with different diameters (refractive index 1.34 and diameters ranging from 5-200 μm) and using a 300 mW laser power with 1 mm diameter and wavelength of 532 nm. The first 10 forward scattering angles are positioned so that they have one-degree resolution at a distance of 200 mm to the scattering center, and the detectors have a diameter of 0.6 mm. The light scattered to the sideward detectors is gathered with parabolic mirrors (diameter of 10 mm) that have a distance of 83 mm to the scattering center. The results of the calculations are shown in Figure 8.

The total scattered intensity measured at a single detector varies three orders of magnitude between ~~the~~ a 5 μm and the 200 μm droplet. Also, the intensity measured at the 18° detector is two orders of magnitude higher than the intensity measured at 90° angle for the same droplet. The calculation for the differential scattering cross section (black and green solid curves) shows oscillation features those are typical for spherical particles. However, these features have a frequency that is significantly higher than the angular resolution of the instrument, and thus cannot be resolved from the measurements. Larger features, like the rainbow between 100° and 120° or decrease in phase function around 100° for a 5 μm droplet and around 130° for 200 μm droplet, can be detected.

Although the MAPMT has a high dynamic range, the electronic processing of the scattering data restricts the resolution of the detection to 11 bits. We simulated the possible response to the electronics assuming ideal optical components with perfect transmission and no crosstalk. The particle size region of interest was chosen to be from 50 μm upward, since at larger particle sizes the imaging ~~part~~ component will provide more information ~~about~~of the particles. We set intensity at the near 90° detector of the 50 μm droplet to be equivalent ~~of~~to 5 counts (assuming that the MAPMT has a background of few counts) and scaled the scattering responses of other droplets respectively. This would represent one gain setting of the MAPMT. From Figure 8 we see that with the proposed gain setting we could detect the scattering phase function of 50 μm and 100 μm droplets ~~from~~over the angular range of 18-170° and the scattering phase function of 200 μm droplets from 42° onwards. In conclusion, we ~~could~~ would be able to image and simultaneously measure the scattering phase function of particle from 50 μm up to almost 200 μm in diameter. It has to be kept in mind that with ice particles we can expect somewhat flatter scattering phase functions, which would increase the measurement range, when measuring in cirrus clouds. By adjusting the MAPMT gain, the measurement range can be shifted to smaller or larger particle sizes.

The forward scattering detectors (1-10°) were positioned to larger distance from the scattering center to get one-degree resolution. The theoretical calculations, however, show that this decreases the intensity in the forward detectors to a degree that the dynamic range of the instrument is not enough to measure the low intensities. To improve this, the forward channels would need a separate MAPMT, whose gain can be adjusted independently of the MAPMT for sideward channels, or the forward channels should be brought to the same distance as the sideward detectors, which would mean that we would give up the one-degree resolution.
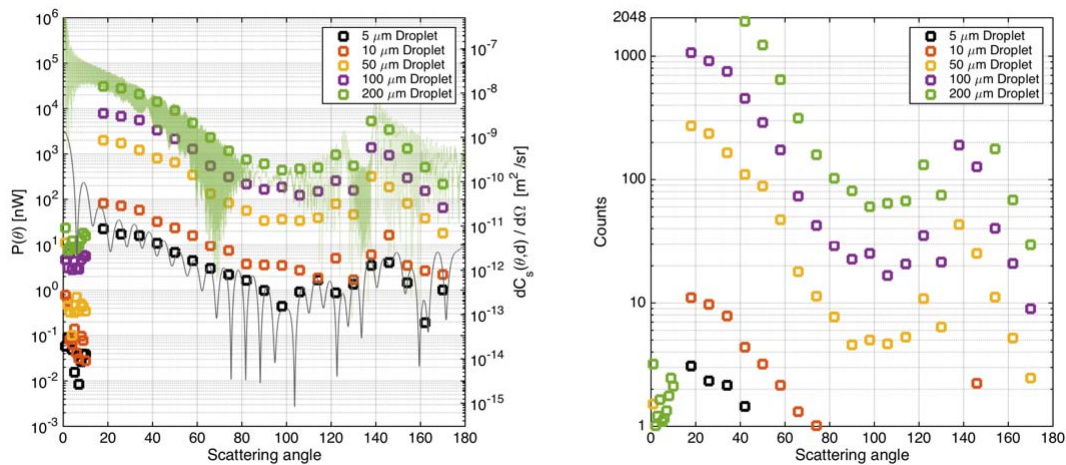

Figure 8: (Left) Theoretical light power that reaches the detectors by laser light scattering on water droplets with diameters of 5 μm (black squares), 10 μm (orange squares), 50 μm (yellow squares), 100 μm (purple squares) and 200 μm (green squares). For 5 μm and 200 μm droplets also the scattering cross sections are shown in high angular resolution. (Right) Digitized particle scattering functions that are expected for a single MAPMT gain setting.

Characterization of PHIPS-HALO with glass bead measurements: Although we focus in this part (Part I) on the design and operation of the probe, we shortly demonstrate here two sample measurements ~~on~~of standard glass beads which were ~~done in purpose of~~used for calibration. An ensemble of glass beads (DRI-CAL, Duke Scientific) ~~is~~ was dispersed with a home-build particle disperser that consists of a small glass bulb equipped with inlet and outlet tubing and allowed to pass through the detection volume. The dispersed glass beads were ~~and is~~

detected by both detection systems. Two standard sizes are used; 19.3 µm ±0.7µm (DC-20) and 49.7µm ±2.0µm (DC-50). The theoretical scattering phase functions of the given size distributions of the two standards were calculated using ~~the~~ Mie-theory and integrated over the solid angles of the detectors (black crosses in Figure 9). The measured scattering phase functions are plotted in solid lines for the 20µm (blue) and 50µm (red) glass

5   beads. The upper panels of Figure 9 a and b show the raw background corrected data before the crosstalk corrections. The 20µm glass beads are used as a reference to define the correction factors for each channel by overlaying the theoretical and measured intensities. We used the 50° as a reference angle and corrected the other measurement angles with respect to it. The obtained correction factors for the individual channels were then used to correct the measured intensities for the 50µm glass beads (red solid line in the lower panel of Figure 9b). The

10   good agreement between the corrected measured intensities and the theoretical values of the 50µm particles validates the crosstalk correction factors.

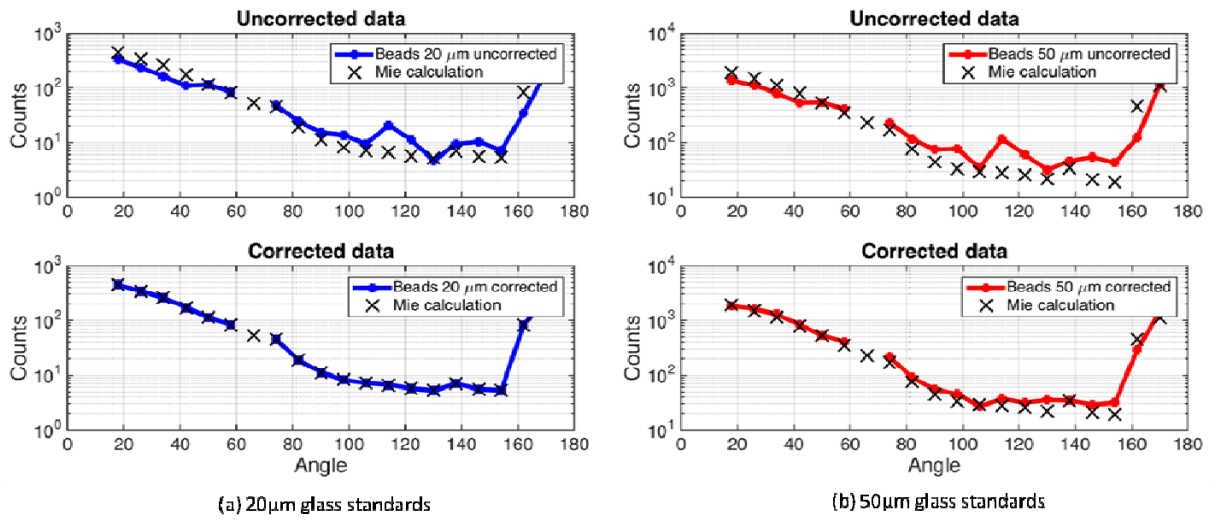
(a) 20µm glass standards   (b) 50µm glass standards

Figure 9 Theoretical (black crosses) and experimental (coloured solid lines) scattering phase functions of two standard glass bead ensembles of 20 µm (blue) and 50 µm (red) diameters. The upper panels show the raw

15   background corrected intensities and the lower panels show the crosstalk corrected intensities. The missing experimental point at 66° is due to a failure in the corresponding physical channel during the measurement.

Although the crosstalk correction factors were determined for spherical particles with a distinct refractive index, it was shown in the study of Schnaiter et al. (2016) that these correction factors also work for ice particles. In

20   that study the PN of the Université Blaise Pascal, Clermont-Ferrand, France was operated parallel to the PHIPS-HALO during AIDA cirrus cloud simulation. The PHIPS-HALO data was corrected with the above determined correction factors and the comparison of measurements revealed a reasonable agreement of the two instruments in simulated ice clouds.

A collection of processed images from the glass bead measurements that were used to characterize the scattering

25   component is shown in Figure 10. The result of the respective image analysis is given in Table 4. For the 50 µm standard both camera-telescope assemblies show a very good agreement with the manufacturer's specifications with deviations clearly within the uncertainty of the glass bead standard. In case of the 20 µm standard, assembly 2 oversizes the beads by 14 to 19% which is in agreement with the results by Schön et al. (2011) for this size

range and which stems from the image analysis procedure. Assembly 1 oversizes the 20 μm beads by additional 15% which can be attributed to the reduced magnification compared to assembly 2. This magnification-dependent oversizing is additionally shown in Figure 11.
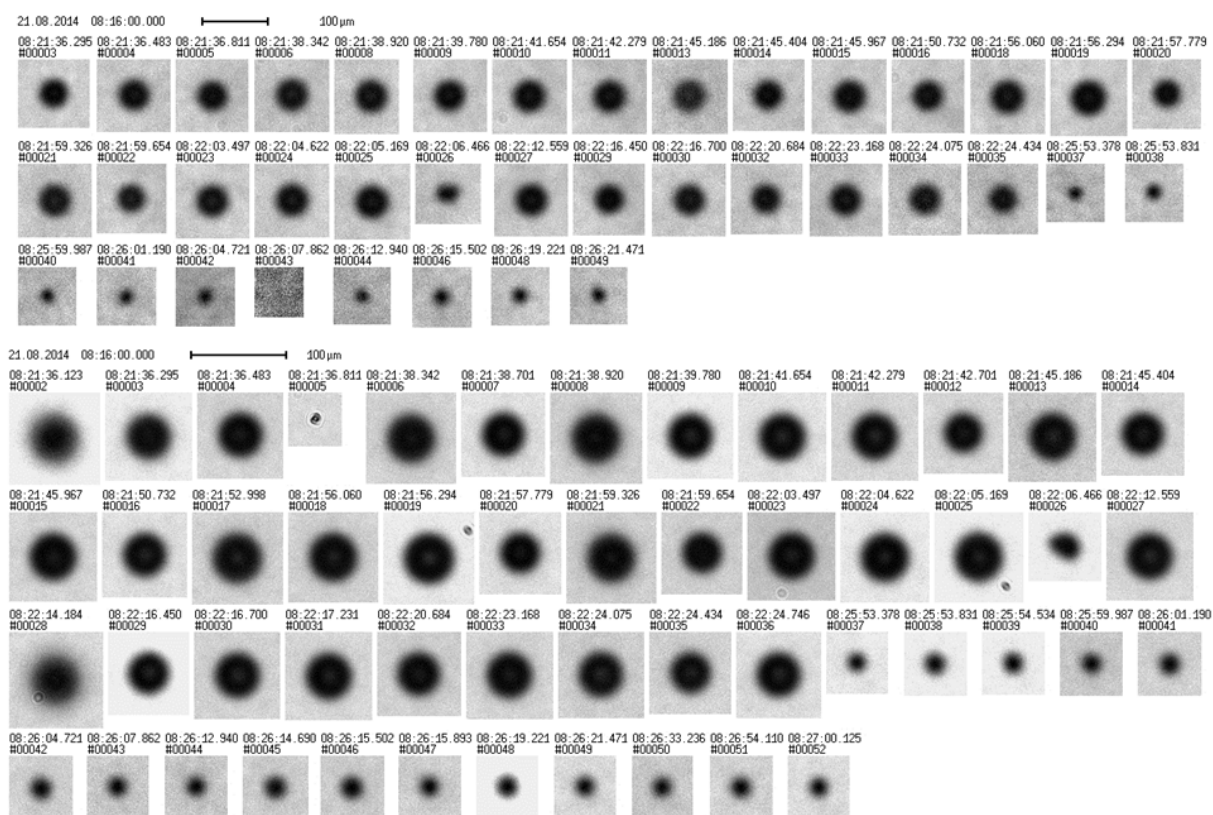

Figure 10 A Series of processed images captured by the camera-telescope assemblies 1 (4 fold magnification, upper panel) and 2 (6 fold magnification, lower panel) for 50 and 20 μm glass bead standards. Note: less than about 1% of all images are empty which sometimes is not recognized by the analysis algorithm (image number 43 in the upper panel). These empty images are especially accepted when dirt particles are present on the telescope optics like in case of image number 5 in the lower panel.

	Manufacturer		Telescope 1 4 fold magnification		Telescope 2 6 fold magnification	
	Mean diameter μm	Std. deviation μm	Mean diameter μm	Std. deviation μm	Mean diameter μm	Std. deviation μm
DRI-CAL 50	49.4 ± 1.6	3.5	49.3	4.1	49.1	4.8
DRI-CAL 20	20.0 ± 0.9	1.9	27.2	1.4	23.9	1.1

Table 4 Statistical results of the image analysis of glass bead standard measurements.
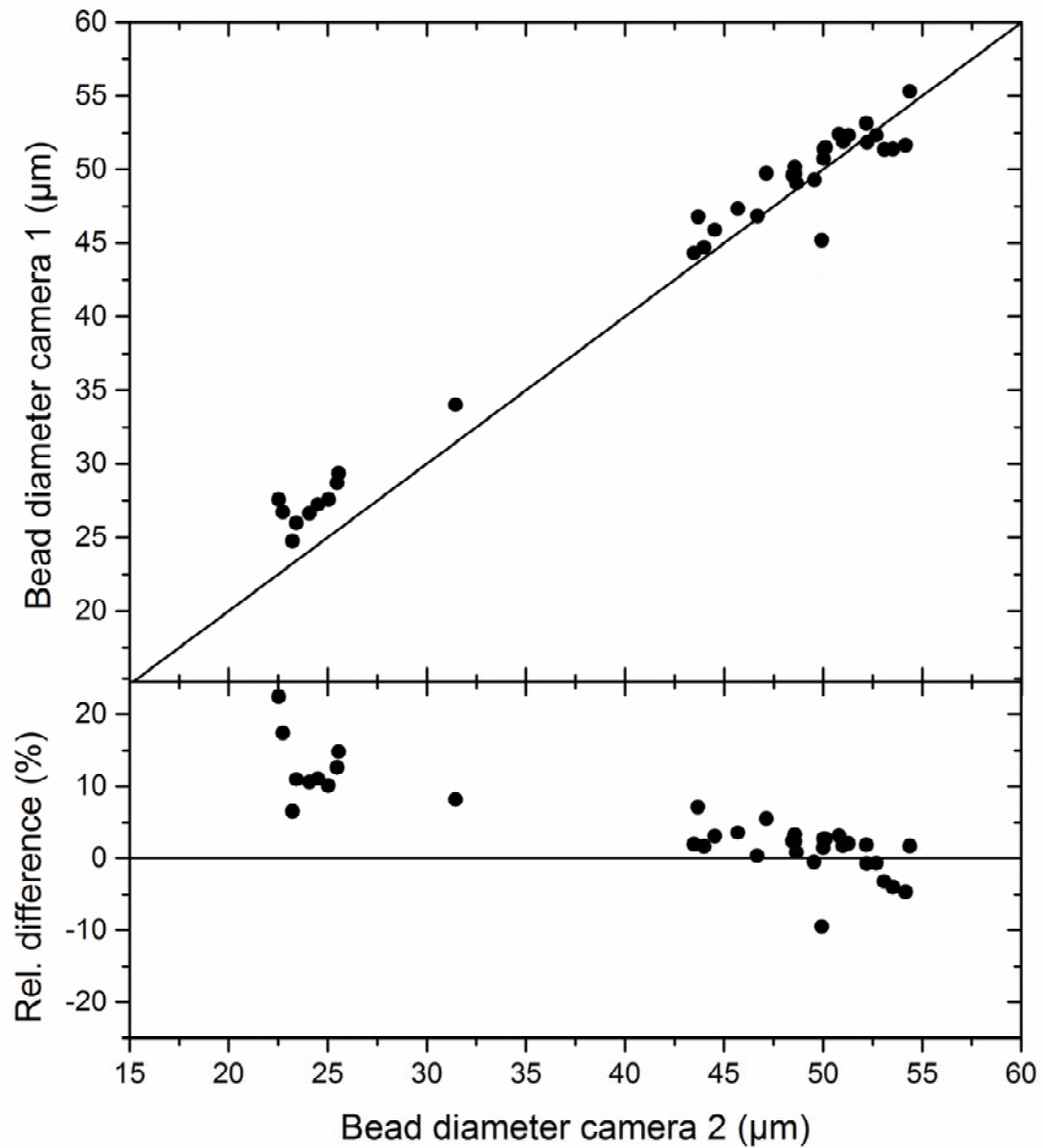
Figure 11 Comparison of the bead diameters deduced from the images of camera-telescope assembly 1 and 2.

6. Summary and outlook

We presented here a novel airborne optical probe (PHIPS-HALO) which is developed at the Karlsruhe Institute for Technology (KIT) to be attached to the German DLR HALO GV-SP aircraft as well as other research aircrafts. The probe is unique in its ability to collect two simultaneous and correlated measurements (the 3D morphology represented in the stereo-image and the corresponding optical properties represented in the polar scattering function of each individual cloud particle. ThereofHence, PHIPS-HALO provides the missing correlation between the cloud particle habit and its scattering properties which are used in radiative transfer models, and can be used as a reference for other airborne cloud-particles-probes applied simultaneously in the same flights. In this part (Part I), we focused on the basic concept of the instrument, the design of the optical head, the electronics and signal processing and the aerodynamic properties. The optical head consists of two

optical systems; 1) The stereo-microscopic imager composed of two camera-telescope assemblies placed after two reflecting mirrors to image the detected particle, with a resolution down to 2.35 μm, at two different viewing angles. The dual imaging configuration produces two shadowgraphic images at two different angles for each detected particle which enables the 3D morphology impression in a similar way ~~of~~ as the human ocular system. Reconstruction of a 3D model for regular shapes like spheres, plates and columns is possible. 2) The polar nephelometer measures the polar scattered light from the cloud particle as it passes across a collimated laser beam. The angular resolution of the differential scattering function is 1° for the forward scattering direction (from 1° to 10°) and 8° for the side and backscattering directions (from 18° to 170°). The scattered signal is transmitted from the scattering plane to a multi-anode photomultiplier via PMMA optical fibers. Optical engineering calculations for the light coupling between the PMMA fiber system and the multi-anode photomultiplier are presented in conjunction with laboratory characterization measurements. These results ~~and showed~~ reveal a ~~potential~~ crosstalk between ~~different~~ adjacent channels ~~of at least 15%~~ up to 20% that needs to be taken into account in the analysis of the polar nephelometer measurements. The crosstalk issue which is discussed here requires the application of cross talk correction factor to the PHIPS data based on a theoretical Mie scattering curve which limits the Phase function data to Mie theory. There is an effort started to redesign the coupling of the signal to the PMT in order to eliminate the crosstalk in future measurements. Detailed signal detection and processing scheme~~s~~ ~~is~~ are discussed. A comprehensive aerodynamic analysis is performed to investigate the mechanical ~~solidity~~ stability of the probe and the possible turbulences at the detection volume. The crucial aerodynamic parameters (flow velocity, Mach number, pressure, temperature, turbulence) are discussed in detail~~s~~ ~~at~~ under a variety of conditions to estimate the mechanical ~~solidity~~ stability of the probe and to verify the geometry for a turbulence-free detection volume. Finally, we modelled the response and detection range of the scattering optics and demonstrated the measurement and crosstalk correction using standard glass beads.

As already mentioned above, ~~T~~ the problem of ~~the~~ crosstalk in the scattering signal requires a better optical design for the fiber-MAPMT coupler. So far, the gain value of the MAPMT can be changed manually only by a mechanical potentiometer on the electronic board of the MAPMT. This ~~should be~~ is now replaced by a digitally controlled potentiometer to allow software access to the gain voltage. Another shortcoming of the MAPMT electronics is that the set gain value applies to all channels. Adjusting the gain to an optimum value which allows detection at all channels but no saturation of signal at any of them is difficult. An access to individual gain for each channel is required. The ~~shuttering~~ shattering of cloud particles at the inlet of the probe is not discussed in part I in details and will be considered in future work in line with field measurements.

References

Abdelmonem, A., Schnaiter, M., Amsler, P., Hesse, E., Meyer, J., and Leisner, T.: First correlated measurements of the shape and light scattering properties of cloud particles using the new Particle Habit Imaging and Polar Scattering (PHIPS) probe, Atmos. Meas. Tech., 4, 2125-2142, 10.5194/amt-4-2125-2011, 2011.

Baum, B. A., Yang, P., Hu, Y.-X., and Feng, Q.: The impact of ice particle roughness on the scattering phase matrix, J. Quant. Spectrosc. Radiat. Transfer, 111, 2534-2549, http://dx.doi.org/10.1016/j.jqsrt.2010.07.008, 2010.

Baumgardner, D., Dye, J. E., Gandrud, B. W., and Knollenberg, R. G.: Interpretation of measurements made by the forward scattering spectrometer probe (FSSP-300) during the Airborne Arctic Stratospheric Expedition, J. Geophys. Res.: Atmos., 97, 8035-8046, 10.1029/91jd02728, 1992.

Baumgardner, D., Jonsson, H., Dawson, W., O'Connor, D., and Newton, R.: The cloud, aerosol and precipitation spectrometer: a new instrument for cloud investigations, Atmos. Res., 59–60, 251-264, http://dx.doi.org/10.1016/S0169-8095(01)00119-3, 2001.

Bi, L., Yang, P., Kattawar, G. W., Hu, Y., and Baum, B. A.: Scattering and absorption of light by ice particles: Solution by a new physical-geometric optics hybrid method, J. Quant. Spectrosc. Radiat. Transfer, 112, 1492-1508, http://dx.doi.org/10.1016/j.jqsrt.2011.02.015, 2011.

Bohren, C. F., and Huffman, D. R.: Introduction, in: Absorption and Scattering of Light by Small Particles, Wiley-VCH Verlag GmbH, 1-11, 2007.

Crépel, O., Gayet, J. F., Fournol, J. F., and Oshchepkov, S.: A new airborne Polar Nephelometer for the measurement of optical and microphysical cloud properties. Part II: Preliminary tests, Ann. Geophys., 15, 460-470, 10.1007/s00585-997-0460-0, 1997.

Draine, B. T., and Flatau, P. J.: Discrete-Dipole Approximation For Scattering Calculations, J. Opt. Soc. Am. A, 11, 1491-1499, 10.1364/josaa.11.001491, 1994.

Fugal, J. P., Shaw, R. A., Saw, E. W., and Sergeyev, A. V.: Airborne digital holographic system for cloud particle measurements, Appl. Opt., 43, 5987-5995, 10.1364/ao.43.005987, 2004.

Gayet, J. F., Crépel, O., Fournol, J. F., and Oshchepkov, S.: A new airborne polar Nephelometer for the measurements of optical and microphysical cloud properties. Part I: Theoretical design, Ann. Geophys., 15, 451-459, 10.1007/s00585-997-0451-1, 1997.

Glen, A., and Brooks, S. D.: A new method for measuring optical scattering properties of atmospherically relevant dusts using the Cloud and Aerosol Spectrometer with Polarization (CASPOL), Atmos. Chem. Phys., 13, 1345-1356, 10.5194/acp-13-1345-2013, 2013.

Glen, A., and Brooks, S. D.: Single Particle Measurements of the Optical Properties of Small Ice Crystals and Heterogeneous Ice Nuclei, Aerosol Sci. Technol., 48, 1123-1132, 10.1080/02786826.2014.963023, 2014.

Havemann, S., and Baran, A. J.: Extension of T-matrix to scattering of electromagnetic plane waves by non-axisymmetric dielectric particles: application to hexagonal ice cylinders, J. Quant. Spectrosc. Radiat. Transfer, 70, 139-158, http://dx.doi.org/10.1016/S0022-4073(00)00127-8, 2001.

Hesse, E., Mc Call, D. S., Ulanowski, Z., Stopford, C., and Kaye, P. H.: Application of RTDF to particles with curved surfaces, J. Quant. Spectrosc. Radiat. Transfer, 110, 1599-1603, http://dx.doi.org/10.1016/j.jqsrt.2009.01.011, 2009.

Jourdan, O., Mioche, G., Garrett, T. J., Schwarzenböck, A., Vidot, J., Xie, Y., Shcherbakov, V., Yang, P., and Gayet, J.-F.: Coupling of the microphysical and optical properties of an Arctic nimbostratus cloud during the ASTAR 2004 experiment: Implications for light-scattering modeling, J. Geophys. Res.: Atmos., 115, D23206, 10.1029/2010jd014016, 2010.

Kaye, P. H., Hirst, E., Greenaway, R. S., Ulanowski, Z., Hesse, E., DeMott, P. J., Saunders, C., and Connolly, P.: Classifying atmospheric ice crystals by spatial light scattering, Opt. Lett., 33, 1545-1547, 10.1364/ol.33.001545, 2008.

Knollenberg, R. G.: The Optical Array: An Alternative to Scattering or Extinction for Airborne Particle Size Determination, Journal of Applied Meteorology, 9, 86-103, 10.1175/1520-0450(1970)009<0086:toaaat>2.0.co;2, 1970.

Korolev, A., Emery, E., and Creelman, K.: Modification and Tests of Particle Probe Tips to Mitigate Effects of Ice Shattering, J. Atmos. Oceanic Technol., 30, 690-708, 10.1175/jtech-d-12-00142.1, 2013.

Lawson, R. P., Baker, B. A., Schmitt, C. G., and Jensen, T. L.: An overview of microphysical properties of Arctic clouds observed in May and July 1998 during FIRE ACE, J. Geophys. Res.: Atmos., 106, 14989-15014, 10.1029/2000jd900789, 2001.

Lawson, R. P., O'Connor, D., Zmarzly, P., Weaver, K., Baker, B., Mo, Q., and Jonsson, H.: The 2D-S (Stereo) Probe: Design and Preliminary Tests of a New Airborne, High-Speed, High-Resolution Particle Imaging Probe, J. Atmos. Oceanic Technol., 23, 1462-1477, 10.1175/jtech1927.1, 2006.

Liu, C., Lee Panetta, R., and Yang, P.: The effects of surface roughness on the scattering properties of hexagonal columns with sizes from the Rayleigh to the geometric optics regimes, J. Quant. Spectrosc. Radiat. Transfer, 129, 169-185, http://dx.doi.org/10.1016/j.jqsrt.2013.06.011, 2013.

Macke, A., Mueller, J., and Raschke, E.: Single Scattering Properties of Atmospheric Ice Crystals, J. Atmos. Sci., 53, 2813-2825, 10.1175/1520-0469(1996)053<2813:sspoai>2.0.co;2, 1996.

Pruppacher, H. R., and Klett, J. D.: in: Microphysics of Cloud and Precipitation Kluwer Academic Publishers, Dordrecht, Netherlands, 954, 1997.

Schnaiter, M., Järvinen, E., Vochezer, P., Abdelmonem, A., Wagner, R., Jourdan, O., Mioche, G., Shcherbakov, V. N., Schmitt, C. G., Tricoli, U., Ulanowski, Z., and Heymsfield, A. J.: Cloud chamber experiments on the origin of ice crystal complexity in cirrus clouds, Atmos. Chem. Phys., 16, 5091-5110, 10.5194/acp-16-5091-2016, 2016.

Schön, R., Schnaiter, M., Ulanowski, Z., Schmitt, C., Benz, S., Möhler, O., Vogt, S., Wagner, R., and Schurath, U.: Particle habit imaging using incoherent light: a first step towards a novel instrument for cloud microphysics, J. Atmos. Oceanic Technol., 10.1175/2010jtecha1445.1, 2011.

Shcherbakov, V., Gayet, J.-F., Baker, B., and Lawson, P.: Light Scattering by Single Natural Ice Crystals, J. Atmos. Sci., 63, 1513-1525, 10.1175/jas3690.1, 2006a.

Shcherbakov, V., Gayet, J.-F., Jourdan, O., Ström, J., and Minikin, A.: Light scattering by single ice crystals of cirrus clouds, Geophys. Res. Lett., 33, L15809, 10.1029/2006gl026055, 2006b.

Shcherbakov, V.: Why the 46° halo is seen far less often than the 22° halo?, J. Quant. Spectrosc. Radiat. Transfer, 124, 37-44, http://dx.doi.org/10.1016/j.jqsrt.2013.03.002, 2013.

Strapp, J. W., Leaitch, W. R., and Liu, P. S. K.: Hydrated and Dried Aerosol-Size-Distribution Measurements from the Particle Measuring Systems FSSP-300 Probe and the Deiced PCASP-100X Probe, J. Atmos. Oceanic Technol., 9, 548-555, 10.1175/1520-0426(1992)009<0548:hadasd>2.0.co;2, 1992.

Ulanowski, Z., Kaye, P. H., Hirst, E., Greenaway, R. S., Cotton, R. J., Hesse, E., and Collier, C. T.: Incidence of rough and irregular atmospheric ice particles from Small Ice Detector 3 measurements, Atmos. Chem. Phys., 14, 1649-1662, 10.5194/acp-14-1649-2014, 2014.

Vochezer, P., Järvinen, E., Wagner, R., Kupiszewski, P., Leisner, T., and Schnaiter, M.: In situ characterization of mixed phase clouds using the Small Ice Detector and the Particle Phase Discriminator, Atmos. Meas. Tech., 9, 159-177, 10.5194/amt-9-159-2016, 2016.

Weigel, R., Spichtinger, P., Mahnke, C., Klingebiel, M., Afchine, A., Petzold, A., Krämer, M., Costa, A., Molleker, S., Jurkat, T., Minikin, A., and Borrmann, S.: Thermodynamic correction of particle concentrations measured by underwing probes on fast flying aircraft, Atmos. Meas. Tech. Discuss., 2015, 13423-13469, 10.5194/amtd-8-13423-2015, 2015.

Yang, P., and Liou, K. N.: Geometric-optics?integral-equation method for light scattering by nonspherical ice crystals, Appl. Opt., 35, 6568-6584, 10.1364/ao.35.006568, 1996.

Yang, P., and Liou, K. N.: T-Matrix Method and its Applications, in: Light scattering by nonspherical particles, edited by: Mishchenko MI, H. J., Travis LD, , Academic Press, New York, 173–221, 1999.

Yurkin, M. A., and Hoekstra, A. G.: The discrete dipole approximation: An overview and recent developments, J. Quant. Spectrosc. Radiat. Transfer, 106, 558-589, http://dx.doi.org/10.1016/j.jqsrt.2007.01.034, 2007.

Figure Captions

Figure 1: Schematic drawing of the optical detection units used in the PHIPS-HALO probe, (a) side view and (b) top view. The main components of the polar nephelometer and stereo-microscopic imager are labelled in blue and red, respectively. The trigger optics links the two components. (c) A real photo of the probe.

Figure 2: Results of optical ~~engineering~~ modeling calculations for the light coupling between the PMMA fiber system and the multi-anode photomultiplier. A crosstalk of at least 15% can be expected that needs to be taken into account in the analysis of the polar nephelometer measurements.

Figure 3 Results of the laboratory characterization of the optical crosstalk within the MAPMT of PHIPS-HALO. The manufacturer given electronic crosstalk between adjacent detectors of 3% is indicated by the shaded area. The deduced optical crosstalk between adjacent detectors is 10% to the left and 20% to the right side indicating a slight misplacement of the fiber coupler with respect to the MAPMT.

Figure 4: Signal detection and processing scheme for a valid particle event at a typical airspeed of 200m/s and at an assumed trigger threshold of 200. The relative distance along the particle trajectory, i.e. the instrument axis, is given on the upper axis. Note, that due to the camera field of view of 1.27 mm along the instrument axis, the imaging system can be aligned in the laboratory by using test particles with particle speeds of only a few m/s.

Figure 5: Mach number distribution (upper panel) and pressure distribution (lower panel) of the flow field inside and outside the probe.

Figure 6: Temperature distribution inside and outside the probe (upper panel) and along the centre line trajectory (lower panel). Incoming particles experience a short-term temperature change of the surrounding air by about 10K within 1 ms at 200 m/s flight speed.

Figure 7: Upper panel: Turbulence Kinetic Energy distribution within the particle flow tube of the probe. The red square marks the detection volume. Lower panel: The TKE along the horizontal centre line trajectory (shown above) is only slightly increased compared to the background value.

Figure 8: (Left) Theoretical light power that reaches the detectors by laser light scattering on water droplets with diameters of 5 μm (black squares), 10 μm (orange squares), 50 μm (yellow squares), 100 μm (purple squares) and 200 μm (green squares). For 5 μm and 200 μm droplets also the scattering cross sections are shown in high angular resolution. (Right) Digitized particle scattering functions that are expected for a single MAPMT gain setting.

Figure 9 Theoretical (black crosses) and experimental (coloured solid lines) scattering phase functions of two standard glass bead ensembles of 20 μm (blue) and 50 μm (red) diameters. The upper panels show the raw background corrected intensities and the lower panels show the crosstalk corrected intensities. The missing experimental point at 66° is due to a failure in the corresponding physical channel during the measurement.

Figure 10 A Series of processed images captured by the camera-telescope assemblies 1 (4 fold magnification, upper panel) and 2 (6 fold magnification, lower panel) for 50 and 20 μm glass bead standards. Note: less than about 1% of all images are empty which sometimes is not recognized by the analysis algorithm (image number 43 in the upper panel). These empty images are especially accepted when dirt particles are present on the telescope optics like in case of image number 5 in the lower panel.

Figure 11 Comparison of the bead diameters deduced from the images of camera-telescope assembly 1 and 2.